

RESEARCH ARTICLE | MARCH 14 2025

# A significant enhancement in thermal conductivity of plastic crystals under compressive strain by deep potential molecular dynamics

Yangjun Qin  ; Zhicheng Zong; Junwei Che  ; Tianhao Li; Haisheng Fang  ; Nuo Yang  

 Check for updates

*Appl. Phys. Lett.* 126, 104101 (2025)

<https://doi.org/10.1063/5.0243420>



## Articles You May Be Interested In

KoopmanLab: Machine learning for solving complex physics equations

*APL Mach. Learn.* (September 2023)

Experimental realization of a quantum classification: Bell state measurement via machine learning

*APL Mach. Learn.* (September 2023)

Nanotechnology & Materials Science


Optics & Photonics

Impedance Analysis

Scanning Probe Microscopy


Sensors

Failure Analysis & Semiconductors



**Unlock the Full Spectrum.**  
From DC to 8.5 GHz.  
Your Application. Measured.

[Find out more](#)



# A significant enhancement in thermal conductivity of plastic crystals under compressive strain by deep potential molecular dynamics

Cite as: Appl. Phys. Lett. **126**, 104101 (2025); doi: [10.1063/5.0243420](https://doi.org/10.1063/5.0243420)

Submitted: 10 October 2024 · Accepted: 15 February 2025 ·

Published Online: 14 March 2025



View Online



Export Citation



CrossMark

Yangjun Qin,<sup>1,2</sup>  Zhicheng Zong,<sup>1,2</sup> Junwei Che,<sup>3</sup>  Tianhao Li,<sup>1,2</sup> Haisheng Fang,<sup>1</sup>  and Nuo Yang<sup>2,a)</sup> 

## AFFILIATIONS

<sup>1</sup>School of Energy and Power Engineering, Huazhong University of Science and Technology, Wuhan 430074, China

<sup>2</sup>Department of Physics, National University of Defense Technology, Changsha 410073, China

<sup>3</sup>Department of Applied Physics, College of Science, Xi'an University of Science and Technology, Xi'an, 710054, China

<sup>a)</sup> Author to whom correspondence should be addressed: [nuo@nudt.edu.cn](mailto:nuo@nudt.edu.cn)

## ABSTRACT

The unique properties of plastic crystals highlight their potential for use in solid-state refrigeration. However, their practical applications are limited by thermal hysteresis due to low thermal conductivity. In this study, the effect of compressive strain on the thermal transport properties of  $[(\text{CH}_3)_4\text{N}][\text{FeCl}_4]$  was investigated using molecular dynamic simulation with a deep potential. It is found that the thermal conductivities along the [100], [010], [001], [101], and [011] directions are enhanced under 9% strain by 110%, 580%, 114%, 408%, and 268%, respectively. The underlying mechanisms are analyzed through vibrational density of states and spectral energy densities. The enhancement in thermal conductivity is primarily due to reduced phonon scattering. These findings offer theoretical insights for the practical application of plastic crystals in thermal management systems.

Published under an exclusive license by AIP Publishing. <https://doi.org/10.1063/5.0243420>

Global warming and carbon neutrality initiatives have driven the demand for advanced technologies in energy harvesting, utilization, and refrigeration.<sup>1</sup> Plastic crystals (PCs) have emerged as a novel and highly promising material for solid-state refrigeration,<sup>2</sup> due to their ability to undergo significant entropy changes during phase transitions in response to variations in temperature and pressure.

PCs exhibit substantial isothermal entropy changes during the barocaloric effect, marked by significant entropy shifts as they transition between ordered and disordered phases. The barocaloric effect<sup>2</sup> offers distinct advantages over conventional refrigeration techniques,<sup>3–5</sup> including reduced driving pressures<sup>6</sup> and enhanced fatigue resistance. For example, neopentyl glycol,<sup>7</sup> a representative organic PC, demonstrates a phase transition enthalpy of up to 389 J/kg/K<sup>2</sup> under a driving pressure of 91 MPa. Alongside neopentyl glycol, other key compounds such as glycerin, pentaerythritol, and tris(hydroxymethyl)aminomethane<sup>8–10</sup> have also shown promise for barocaloric applications. The pronounced isothermal entropy change in PCs is primarily driven by the formation and dissociation of hydrogen bonds during the phase transition.<sup>11</sup> However, the disordered structure of PCs usually results in significant phonon scattering, which lowers thermal conductivity and increases thermal hysteresis.<sup>12,13</sup>

Since the magnitude of thermal hysteresis directly affects refrigeration efficiency, balancing optimal phase transition performance with the minimization of thermal hysteresis remains a critical challenge in advancing solid-state refrigeration technologies.

Generally, there are some methods to improve the thermal conductivity of PCs, including strain modulation,<sup>11,14</sup> electric field modulation,<sup>15</sup> and doping modulation.<sup>16,17</sup> Pressure modulation alters the molecular arrangement and interactions within the crystal, resulting in a more compact structure that reduces phonon scattering and improves thermal conductivity. For instance, Wang *et al.* demonstrated a threefold increase in the in-plane thermal conductivity of pentaerythritol under a pressure of 3.5 GPa.<sup>18</sup> while Li *et al.* observed a 10% enhancement in the thermal conductivity of neopentyl glycol at 0.2 GPa.<sup>11</sup> Electric field modulation has also shown promise; Deng *et al.* reported a 53% increase in thermal conductivity of vinylidene fluoride through electric field polarization,<sup>15</sup> which improves system ordering, reduces phonon scattering, and increases group velocity. Doping modulation, which involves introducing alternative molecules or atoms to modify the composition and structure of plastic crystals, can influence phonon scattering and thermal conductivity.<sup>16</sup> However, this method can also affect the phase transition properties of the PCs.

Notably,  $[(\text{CH}_3)_4\text{N}][\text{FeCl}_4]$ <sup>19</sup> is a typical ionic crystal with the properties of PCs and ferroelectric material with applications in various fields. Despite this, the effects of strain on ionic PCs remain relatively unexplored, underscoring the need for further investigation.

The deep potential (DP)<sup>20–23</sup> molecular dynamics (MD) is a powerful tool to study the physic properties and uncover the microscopic mechanism. It combines the accuracy of density functional theory (DFT)<sup>24,25</sup> with the computational efficiency of classical MD. The reliability of this method has been validated across various systems,<sup>26</sup> including ferroelectric, semiconductor,<sup>27</sup> ionic,<sup>28</sup> high-entropy alloy, and organic systems.<sup>24,29–31</sup> Therefore, the application of deep neural network models can provide critical insights into the mechanisms underlying heat transport in these materials.

This work developed a deep potential for plastic crystal  $[(\text{CH}_3)_4\text{N}][\text{FeCl}_4]$  to explore the effect of compressive strain along different directions on the thermal transport properties using the DPMD.<sup>32,33</sup> First, the accuracy of the potential function was validated by comparing results from DFT and DP. Second, the thermal conductivity of PCs was evaluated under varying strains applied along three directions. Finally, the vibrational density of states (vDOS) and the normalized spectral energy density (SED) distributions were calculated to further characterize the system. The primary aim was to investigate phonon transport properties under different strain conditions. This study provides critical insights into the regulation of thermal conductivity in PCs through strain engineering.

Deep learning models<sup>22,34</sup> are utilized to automatically extract complex features and patterns from large volumes of data through multiple layers of nonlinear transformations. The model comprises multiple hidden layers, with each layer comprising several neurons. Each neuron in a given layer is connected to all neurons in subsequent layers, thereby enabling fully connected neural networks to learn complex nonlinear mapping relationships. Additionally, within the DP model, the process of mapping converts the positional data of atoms into feature vectors and descriptors, which represent the local environment surrounding each atom. Each local environment  $E_i$  comprises the contribution of the respective atom and its neighboring atoms, and the total energy of the system is obtained by means of accumulation.

The DP of  $[(\text{CH}_3)_4\text{N}][\text{FeCl}_4]$ , comprising four phases, was developed using deep potential generator (DP-GEN)<sup>34,35</sup> in a closed-loop automated approach. The DP-GEN framework iteratively explores the configurational space through three key steps: training, exploration, and labeling. The initial dataset was generated by perturbing the four phases of the crystal and performing *ab initio* molecular dynamics (AIMD). Such calculations were performed based on the density functional theory (DFT) implemented in the Vienna *ab initio* simulation package (VASP), in which the Perdew–Burke–Ernzerhof (PBE) generalized gradient approximation (GGA) and projector augmented wave (PAW) pseudopotentials were applied. As detailed in Fig. S2, the energy cutoff and k-point spacing were set to 520 eV and 0.4, respectively, ensuring accurate results.

After obtaining the initial data, four DP models were trained using different random numbers. More details of the methodology can be referred to in the [supplementary material](#). In the exploration step, the structural phase space was explored through MD simulation utilizing the large-scale atomic/Molecular Massively Parallel Simulator (LAMMPS),<sup>36–38</sup> which were conducted at various temperatures and pressures across different phase structures using the isothermal-isobaric

(NPT) ensemble. In the labeling step, the remaining three potential functions were evaluated by comparing their predictions for energy, force, and virial properties. Structures with the highest force deviations were specifically selected for analysis

$$\delta_f^{\max} = \max_i \sqrt{\langle |F_i - \langle F_i \rangle|^2 \rangle}. \quad (1)$$

When  $\delta_{low} < \delta_f^{\max} < \delta_{high}$ , the configuration is labeled as a candidate configuration, and added to the initial dataset for training in the next iteration. The iterative process constitutes until the accuracy of the potential function reaches 99%. The distribution of the final maximum force deviation is shown in Fig. S1. Throughout the multiple iterations, approximately  $0.4 \times 10^6$  phase space structures were explored.

Once a high-accuracy potential function is established, the energy and force data of both the training and test were compared in Fig. 1. A strong linear correlation between the DP and DFT data are evident in Figs. 1(a) and 1(b), confirming the high accuracy of the potential function. Additionally, the phase IV cell, containing 44 atoms in Fig. 1(d), was used to calculate the dispersion curve using the phonopy<sup>39</sup> software to generate a  $3 \times 3 \times 3$  supercell with 1188 atoms. Calculating this using the finite displacement method is exceedingly challenging and impractical. Therefore, the energy profile of the fourth phase was calculated independently and found to be in excellent agreement with DFT in Fig. 1(c). This confirms the accuracy of potential function and its suitability for calculating the properties of plastic crystals.

The thermal conductivity  $\kappa$  was calculated using the equilibrium molecular dynamics (EMD) method based on the Green–Kubo formula,<sup>40</sup>

$$\kappa = \frac{V}{3k_B T^2} \int_0^\infty \langle J(0)J(t) \rangle dt, \quad (2)$$

where  $\langle J(0)J(t) \rangle$  is the heat current autocorrelation function (HCACF),  $k_B$  is Boltzmann constant,  $T$  is the temperature, and  $V$  is the volume of the simulation cell.

The heat current  $J$  was calculated using the following expression:

$$J = \frac{1}{V} \left[ \sum_i e_i v_i + \frac{1}{2} \sum_{i<j} (F_{ij} \cdot (v_i + v_j)) r_{ij} \right], \quad (3)$$

where  $e_i$ ,  $v_i$ ,  $r_{ij}$ , and  $F_{ij}$  are the energy, velocity, position vector, and force, respectively.

The vDOS was calculated from the Fourier transform of the velocity autocorrelation function,

$$vDOS = \int_0^{\tau_0} \frac{v(0) \cdot v(t)}{v(0) \cdot v(0)} \exp(-2\pi i \omega t) dt, \quad (4)$$

where  $\tau_0$  is the simulation time and  $v$  is the velocity of atoms.

The formula for SED<sup>41–44</sup> determines the distribution of the vibrational energy in the wavevector–frequency space, calculated from the following expression:

$$\Phi(\mathbf{k}, \omega) = \frac{1}{4\pi\tau_0 N_T} \sum_\alpha \sum_b^B m_b \left| \int_0^{\tau_0} \sum_{n_{x,y,z}} u_x \left( \begin{matrix} n_{x,y,z} \\ b \end{matrix}; t \right) \times \exp \left[ i\mathbf{k} \cdot \mathbf{r} \left( \begin{matrix} n_{x,y,z} \\ 0 \end{matrix} \right) - i\omega t \right] dt \right|^2, \quad (5)$$

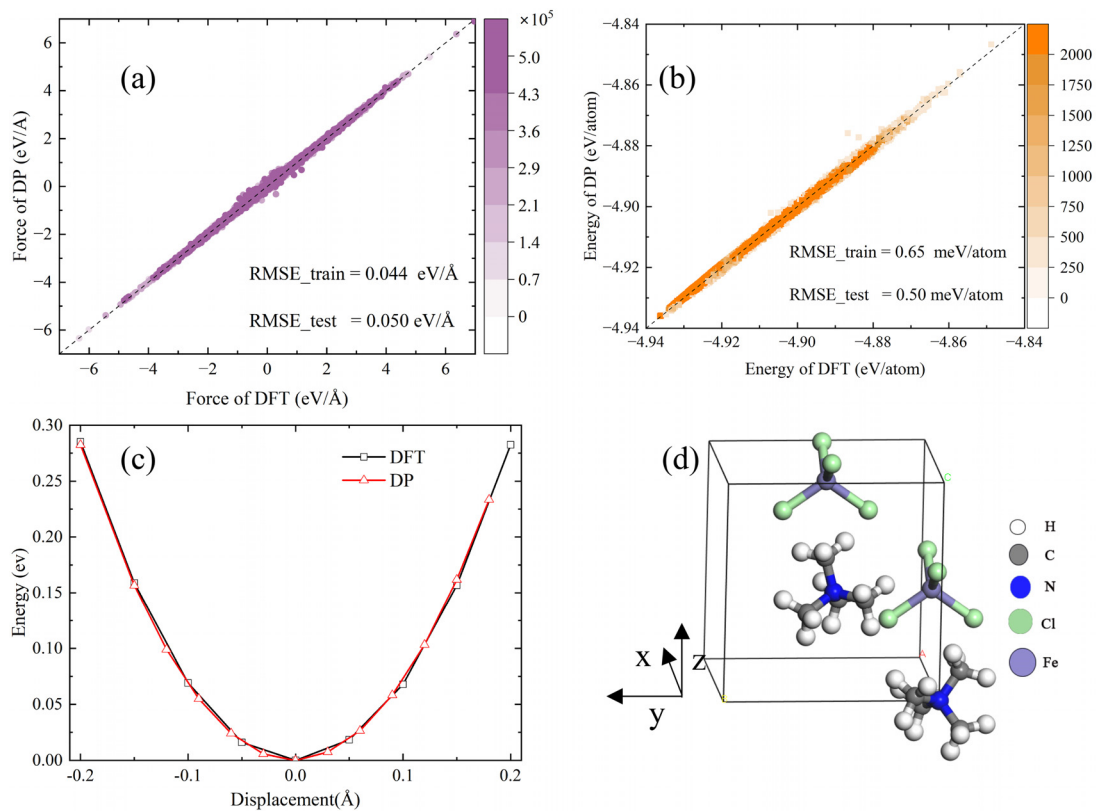


**FIG. 1.** Training and validation results of deep potential. (a) Comparison of forces calculated by the DP and DFT. (b) Comparison of energies calculated by the DP and DFT. (c) A comparison is presented of the energies obtained by DFT and DPMD, the horizontal coordinate denotes the offset of the Fe atom along [100] from its equilibrium position, while the vertical coordinate signifies the extent of change in the system energy. (d) Schematic structure of the system as visualized with OVITO.<sup>45</sup>

where  $N_T$  represents the number of unit cells in PCs,  $n_{x,y,z}$ ,  $B$ ,  $m_b$ , and  $u_\alpha$  are the number of the protocells, the total number of atoms in the protocells, the masses of the atoms, and the velocities in the direction  $\alpha$ , with the velocities being taken to be  $x$ ,  $y$ , and  $z$ , respectively.  $\mathbf{r}$  is the vector of displacements from the origin to the protocells.

The impact of strain along three different directions on the potential energy and volume of PCs was calculated and compared using both DPMD and traditional universal force field consistent valence force field MD (UFF-CVFF MD) in Fig. 2. The initial structural configuration in the absence of strain is presented in Fig. 2(a). The detailed relaxation and simulation parameters are provided in detail as supplementary material III.

Figure 2(b) reveals the potential energies along the [100], [010], and [001] directions exhibit a trend of initially increasing and then decreasing with increasing strain. This indicates that the imposition of compressive strains reduces the stability of  $[(\text{CH}_3)_4\text{N}][\text{FeCl}_4]$  until it reaches a critical peak, beyond which the system collapses under external forces.

Meanwhile, it is observed that the potential energy tends to decrease slowly and then increase using UFF-CVFF, accompanied by continuous volume reduction in Fig. 2(c). These discrepancies highlight the superior accuracy of DPMD in capturing strain-dependent behavior. A comparison of the trends across the three directions highlights significant anisotropy in  $[(\text{CH}_3)_4\text{N}][\text{FeCl}_4]$ .

Corresponding to Fig. 2(b), Fig. 2(d) shows that the volume undergoes gradual reduction followed by expansion under compressive strain. Then, the system collapses after a critical value of compressive strain.

The effect of strain on the thermal conductivity of plastic crystals in different orientations was also investigated. The thermal conductivity for various orientations and strain levels are presented in Figs. 3(a)–3(d) and compared with available experimental data.<sup>46</sup> Thermal conductivity was calculated averaging the results of ten calculations after the HCACF stabilized, as shown in Fig. S8(d).

As shown in Figs. 3(a)–3(d), in the absence of strain, the thermal conductivity of  $[(\text{CH}_3)_4\text{N}][\text{FeCl}_4]$  by DPMD is 0.19, 0.14, and 0.35 W/m-K along [100], [010], and [001], respectively. In Ref. 46, the thin films of  $[(\text{CH}_3)_4\text{N}][\text{FeCl}_4]$  (67  $\mu\text{m}$  in thick) are prepared and measured that the values of thermal conductivity along the in-plane direction ([100] and [010]) and the cross-plane direction ([001]) are 0.32 and 0.24 W/m-K, respectively, which is in close alignment with those obtained by DPMD.

The thermal conductivity of  $[(\text{CH}_3)_4\text{N}][\text{FeCl}_4]$  was further evaluated under compressive strain along three different orientations. For compressive strain along the [100] direction [Fig. 3(a)], the effect of compressive strain on thermal conductivity was not significant, aligning with the observed changes in strain and volume. In addition, for strain applied along the [010] direction [Fig. 3(b)], it leads to a

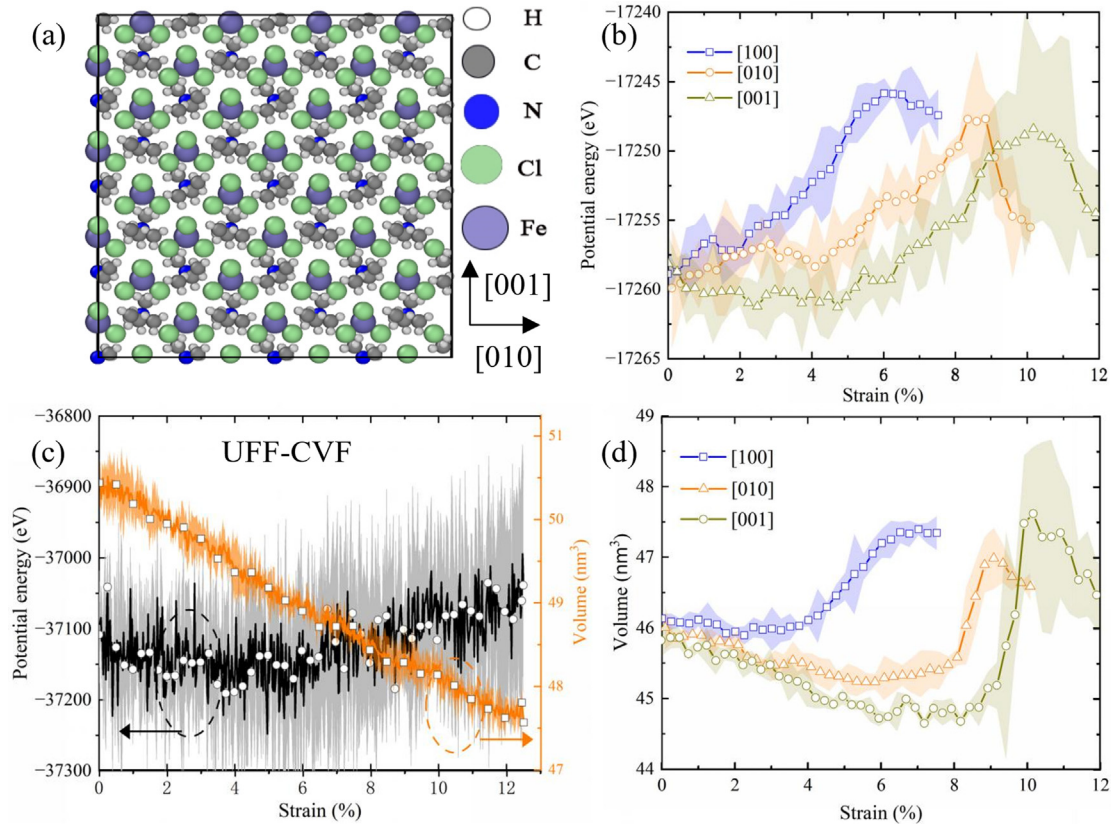


**FIG. 2.** (a) The potential energy diagrams along different directions of strain using DPMD. (b) The volume and potential energy diagrams along different directions of strain using UFF-CVFF. (c) The volume diagrams along different directions of strain using DPMD. (d) The structural diagram at 0% strain for different plane using DPMD. The shadow area is the error band.

significant increase in thermal conductivity, with respective increases of 69%, 168%, and 8% along the [100], [010], and [001] directions, respectively.

Notably, strain along the [001] direction [Fig. 3(c)] results in an initial decrease in thermal conductivity, followed by a subsequent increase across all directions. Notably, thermal conductivity increased by up to 110%, 580%, 114%, 44.9%, 408%, and 267% along the [100], [010], [001], [110], [101], and [011] direction, respectively.

In addition, a comparison of thermal conductivity is presented using the UFF-CVFF MD and DPMD methods in Fig. 3(d). In contrast, the result of DPMD demonstrates a greater proximity to the experimental data. The disparity between the experimental and calculated values can be attributed to the presence of grain boundaries, domain walls, and other structural features in the experimental material, which increase phonon scattering and reduce the overall thermal conductivity. As shown in Fig. S8(b), the thermal conductivity under compressed strain along the [001] direction is also calculated and compared by UFF-CVFF MD and DPMD. The results of classical force field MD do not exhibit a significant thermal conductivity enhancement.

To gain deeper insight into the mechanism by which strain affects thermal conductivity, the vDOS and normalized SED were calculated. Figure 4 illustrates the distribution of phonon mode in the  $[(\text{CH}_3)_4\text{N}]$

$[\text{FeCl}_4]$  under various strain conditions. It can be seen that the most of phonon modes occur at frequencies below 50 THz, with additional modes near 90 THz attributed to the hydrogen atoms, whose lower mass leads to in higher vibrational frequencies. Interestingly, the number of phonon modes at different frequencies remains largely unchanged under strain, irrespective of direction, indicating that the system maintains its structural stability and integrity. In crystals, low-frequency phonon modes play a significant role in determining thermal conductivity. As shown in Fig. 4, in the low-frequency range, increasing strain leads to peak broadening, a blue shift in peak position, and an increase in group velocity—all of which enhance phonon transport. These changes collectively result in increased thermal conductivity within the system.

In addition to phonon modes, the phonon-phonon scattering is a key factor to determine thermal conductivity. The phonon spectral energy density (SED) is an essential tool for investigating and analyzing phonon behavior in materials.<sup>47</sup> The SED is obtained through a two-dimensional Fourier transform of the atomic velocity field, enabling it to capture a wide range of dynamic features at various temperatures and to effectively incorporate the effects of anharmonic interactions on phonon modes. With the calculation of SED, it is obtained that the lifetimes of individual phonon modes in complex structures under finite temperature conditions. This method also

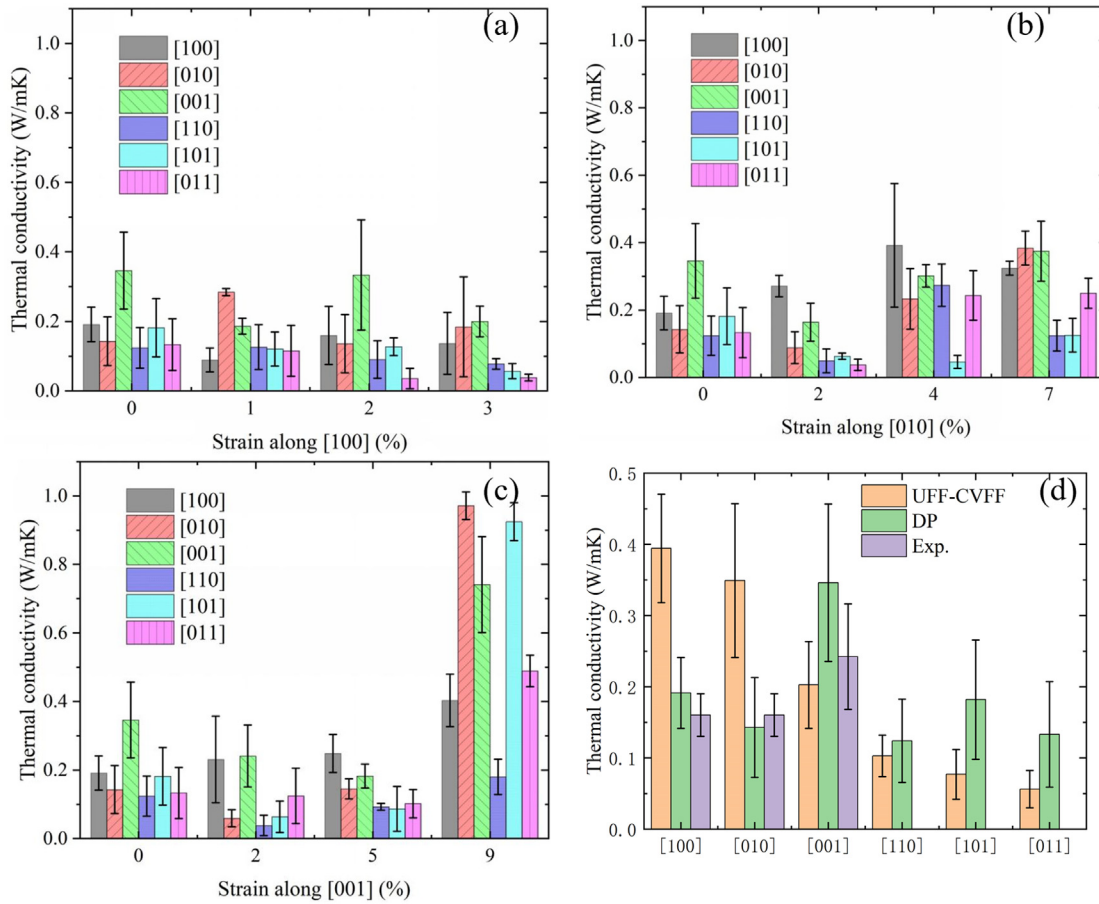


**FIG. 3.** Thermal conductivity of PCs under the different strains. (a)–(c) The thermal conductivity of PCs along the [100], [010], [001], [110], [101], and [011] directions under different strains. The violet triangles are experimental values for thermal conductivity averaged in three directions. (d) Comparison of thermal conductivity in different directions calculated by UFF-CVFF MD, DPMD, and Exp.<sup>46</sup> under 0% strain.

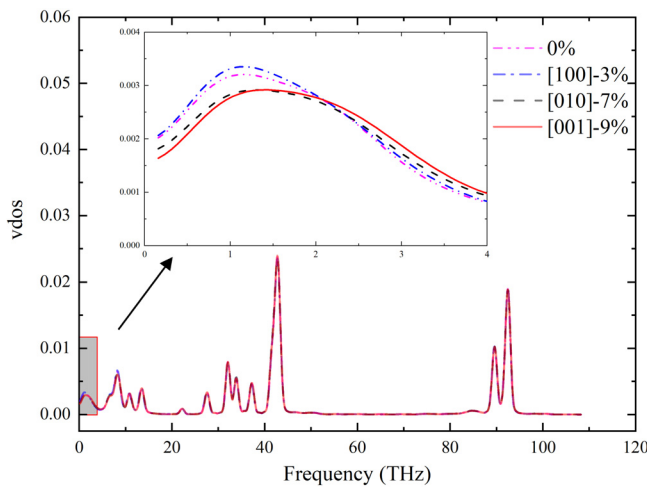


**FIG. 4.** The vDOS of PCs with different strains.

accounts for the anharmonic effects of atomic interactions at thermal equilibrium.

In addition to phonon modes, phonon scattering between individual modes is a key factor to determine thermal conductivity. To explore this effect, the SED distribution of  $[(\text{CH}_3)_4\text{N}][\text{FeCl}_4]$  was calculated for strains within 0–1 THz frequency range. Figure 5 presents the SED distribution at different strain levels, with frequency values displayed on the left and energy values on the right. Obviously, the system exhibits pronounced anharmonicity, which, combined with the presence of numerous protocell atoms, leads to significant phonon scattering, which accounts for the low thermal conductivity. Due to such a strong phonon scattering, distinct phonon modes are difficult to discern in Fig. 5. At strains of [010]-7% and [001]-9%, the SED shows increased vibrational energies in the low-frequency region, which corresponds to enhanced thermal conductivity. In contrast, at [010]-7% strain, the SED is more obscured, indicating increased phonon scattering, as seen in Fig. 5 and Fig. S3. This explains the reduction in thermal conductivity along the [010] direction compared to the

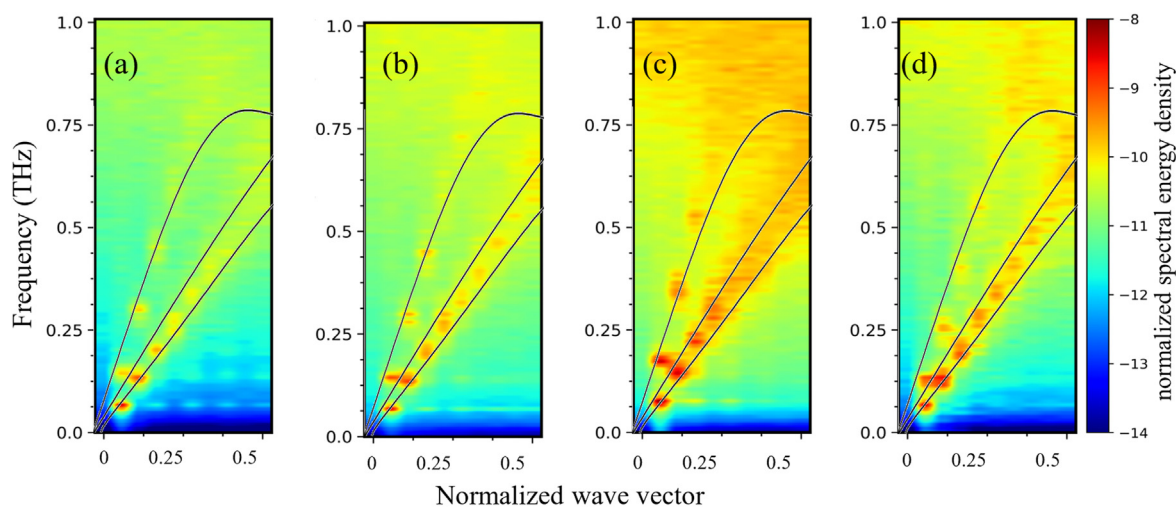


**FIG. 5.** (a)–(d) The normalized SED of PCs with a strain of 0%, 3% ([100] direction), 7% ([010] direction), and 9% ([001] direction) at 0–1 THz. The black solid lines are the acoustic branches under 0% strain calculated by phonopy.<sup>39</sup>

[001] direction at 7% strain. The differences in phonon scattering and energy distribution at various strain levels also highlight the complex interplay between strain and phonon transport in determining thermal conductivity.

The MSD demonstrates a tendency to fluctuate around a specific value, a behavior that is characteristic of crystals. The MSD distributions for different atoms in the absence of strain are depicted in Fig. S9 and analyzed in [supplementary material IV](#).

In conclusion, a deep neural network potential model was developed to study the heat transport properties of  $[(\text{CH}_3)_4\text{N}][\text{FeCl}_4]$  under varying strains. The deep potential was highly accurate, closely matching results from DFT calculations.

The thermal conductivity was computed by using DPMD and UFF-CVFF MD. Notably, a 9% strain along the [001] direction resulted in an increase in 580%, 114%, 408%, and 267% along the [010], [001], [101], and [011] directions, respectively. Conversely, classical force fields have been observed to exert minimal boosting effects. To further investigate the mechanism by which strain impacts heat transport, the vDOS and SED were calculated. The findings revealed that high strain enhances low-frequency phonon modes, increases group velocity, and reduces phonon scattering.

These findings not only enhance the understanding of the heat transport in ferroelectric and plastic crystals under tensile stress but also offer guidance for future applications in thermal management and refrigeration systems.

See the [supplementary material](#) for more details on specific potential function training and comparisons of UFF-CVFF MD, DPMD, etc. There are no conflicts of interest to declare.

This work was financially supported by the National Key Research and Development Project of China, No. 2018YFE0127800. The work was carried out at the National Supercomputer Center in Tianjin, and the calculations were performed on the Tianhe new generation supercomputer.

## AUTHOR DECLARATIONS

### Conflict of Interest

The authors have no conflicts to disclose.

### Author Contributions

**Yangjun Qin:** Data curation (lead); Formal analysis (lead); Investigation (lead); Writing – original draft (lead). **Zhicheng Zong:** Investigation (equal); Software (equal). **Junwei Che:** Data curation (equal); Investigation (equal); Writing – review & editing (supporting). **Tianhao Li:** Investigation (supporting); Software (supporting). **Haisheng Fang:** Investigation (supporting). **Nuo Yang:** Conceptualization (equal); Project administration (equal); Writing – review & editing (equal).

## DATA AVAILABILITY

The data that support the findings of this study are available from the corresponding author upon reasonable request.

## REFERENCES

- <sup>1</sup>H. Xu, “Facilitating full and effective implementation of the Paris Agreement for carbon neutrality vision,” *Carbon Neutrality* **1**(1), 3 (2022).
- <sup>2</sup>B. Li, Y. Kawakita, S. Ohira-Kawamura *et al.*, “Colossal barocaloric effects in plastic crystals,” *Nature* **567**(7749), 506–510 (2019).
- <sup>3</sup>B. G. Shen, J. R. Sun, F. X. Hu *et al.*, “Recent progress in exploring magneto-caloric materials,” *Adv. Mater.* **21**(45), 4545–4564 (2009).
- <sup>4</sup>Y. Nouchokgwe, P. Lheritier, C.-H. Hong *et al.*, “Giant electrocaloric materials energy efficiency in highly ordered lead scandium tantalate,” *Nat. Commun.* **12**(1), 3298 (2021).
- <sup>5</sup>L. Mañosa and A. Planes, “Materials with giant mechanocaloric effects: Cooling by strength,” *Adv. Mater.* **29**(11), 1603607 (2017).
- <sup>6</sup>Q. Ren, J. Qi, D. Yu *et al.*, “Ultrasensitive barocaloric material for room-temperature solid-state refrigeration,” *Nat. Commun.* **13**(1), 2293 (2022).
- <sup>7</sup>F. B. Li, M. Li, X. Xu *et al.*, “Understanding colossal barocaloric effects in plastic crystals,” *Nat. Commun.* **11**(1), 4190 (2020).
- <sup>8</sup>D. Chandra, W. Ding, R. A. Lynch *et al.*, “Phase transitions in ‘plastic crystals,’” *J. Less Common Met.* **168**(1), 159–167 (1991).

- <sup>9</sup>L. W. Breed and E. Murrill, "Solid-solid phase transitions determined by differential scanning calorimetry. III. Organosilicon compounds," *Inorg. Chem.* **10**(3), 641–643 (1971).
- <sup>10</sup>J. L. Tamarit, M. A. Pérez-Jubindo, and M. Fuente, "Dielectric studies on orientationally disordered phases of neopentylglycol (and tris(hydroxymethyl aminomethane)," *J. Phys.: Condens. Matter* **9**(25), 5469 (1997).
- <sup>11</sup>F. Li, M. Li, C. Niu *et al.*, "Atomic-scale insights into the colossal barocaloric effects of neopentyl glycol plastic crystals," *Appl. Phys. Lett.* **120**(7), 073902 (2022).
- <sup>12</sup>M. Kaviany, *Heat Transfer Physics* (Cambridge University Press, 2008).
- <sup>13</sup>S. Wang, L. Sun, B. Li *et al.*, "Atomistic insights into the anisotropic and low thermal conductivity in neopentyl glycol crystals: A molecular dynamics study," *J. Phys. Chem. C* **125**(29), 15853–15862 (2021).
- <sup>14</sup>J. He, C. Yu, S. Lu *et al.*, "Complex role of strain engineering of lattice thermal conductivity in hydrogenated graphene-like borophene induced by high-order phonon anharmonicity," *Nanotechnology* **35**(2), 025703 (2024).
- <sup>15</sup>S. Deng, D. Ma, G. Zhang *et al.*, "Modulating the thermal conductivity of crystalline nylon by tuning hydrogen bonds through structure poling," *J. Mater. Chem. A* **9**(43), 24472–24479 (2021).
- <sup>16</sup>F. Li, C. Niu, X. Xu *et al.*, "The effect of defect and substitution on barocaloric performance of neopentylglycol plastic crystals," *Appl. Phys. Lett.* **121**(22), 223902 (2022).
- <sup>17</sup>Y. Liu, H. Zhou, Z. Xu *et al.*, "Giant barocaloric effect in neopentylglycol-graphene nanosheets composites with large thermal conductivity," *Mater. Res. Lett.* **10**(10), 675–681 (2022).
- <sup>18</sup>S. Wang, H. Fan, Z. Zhang *et al.*, "Resonant phonon modes induced by molecular rotations in  $\alpha$ -pentaerythritol crystals," *J. Mater. Chem. C* **10**(39), 14431–14438 (2022).
- <sup>19</sup>J. Harada, N. Yoneyama, S. Yokokura *et al.*, "Ferroelectricity and piezoelectricity in free-standing polycrystalline films of plastic crystals," *J. Am. Chem. Soc.* **140**(1), 346–354 (2018).
- <sup>20</sup>T. Wen, L. Zhang, H. Wang *et al.*, "Deep potentials for materials science," *Mater. Futures* **1**(2), 022601 (2022).
- <sup>21</sup>D. Tisi, L. Zhang, R. Bertossa *et al.*, "Heat transport in liquid water from first-principles and deep neural network simulations," *Phys. Rev. B* **104**(22), 224202 (2021).
- <sup>22</sup>J. Zeng, D. Zhang, D. Lu *et al.*, "DeePMD-kit v2: A software package for deep potential models," *J. Chem. Phys.* **159**(5), 054801 (2023).
- <sup>23</sup>R. He, H. Wu, L. Zhang *et al.*, "Structural phase transitions in SrTiO<sub>3</sub> from deep potential molecular dynamics," *Phys. Rev. B* **105**(6), 064104 (2022).
- <sup>24</sup>L. Zhang, H. Wang, R. Car *et al.*, "Phase diagram of a deep potential water model," *Phys. Rev. Lett.* **126**(23), 236001 (2021).
- <sup>25</sup>W. Zhao, H. Qiu, and W. Guo, "A deep neural network potential for water confined in graphene nanocapillaries," *J. Phys. Chem. C* **126**(25), 10546–10553 (2022).
- <sup>26</sup>O. Yulou, Z. Zhongwei, Y. Cuiqian *et al.*, "Accuracy of machine learning potential for predictions of multiple-target physical properties," *Chin. Phys. Lett.* **37**(12), 126301–126301 (2020).
- <sup>27</sup>Y. Ouyang, C. Yu, J. He *et al.*, "Accurate description of high-order phonon anharmonicity and lattice thermal conductivity from molecular dynamics simulations with machine learning potential," *Phys. Rev. B* **105**(11), 115202 (2022).
- <sup>28</sup>X. W. Yangjun Qin, L. Mu, Z. Zong, T. Li, and N. Yang, "Deep potential for interaction between hydrated Cs<sup>+</sup> and graphene," [arXiv:2408.15797](https://arxiv.org/abs/2408.15797) (2024).
- <sup>29</sup>L. Zhang, D.-Y. Lin, H. Wang *et al.*, "Active learning of uniformly accurate interatomic potentials for materials simulation," *Phys. Rev. Mater.* **3**(2), 023804 (2019).
- <sup>30</sup>J. Wu, E. Zhou, A. Huang *et al.*, "Deep-potential enabled multiscale simulation of gallium nitride devices on boron arsenide cooling substrates," *Nat. Commun.* **15**(1), 2540 (2024).
- <sup>31</sup>Y. Shi, R. He, B. Zhang *et al.*, "Revisiting the phase diagram and piezoelectricity of lead zirconate titanate from first principles," *Phys. Rev. B* **109**(17), 174104 (2024).
- <sup>32</sup>X. Wan, D. Ma, D. Pan *et al.*, "Optimizing thermal transport in graphene nanoribbon based on phonon resonance hybridization," *Mater. Today Phys.* **20**, 100445 (2021).
- <sup>33</sup>W. Gao, L. Shen, S. Sun *et al.*, "Forecasting solar still performance from conventional weather data variation by machine learning method," *Chin. Phys. B* **32**(4), 048801 (2023).
- <sup>34</sup>Y. Zhang, H. Wang, W. Chen *et al.*, "DP-GEN: A concurrent learning platform for the generation of reliable deep learning based potential energy models," *Comput. Phys. Commun.* **253**, 107206 (2020).
- <sup>35</sup>K. Li, D. Persaud, K. Choudhary *et al.*, "Exploiting redundancy in large materials datasets for efficient machine learning with less data," *Nat. Commun.* **14**(1), 7283 (2023).
- <sup>36</sup>Y. Qin, J. Zhao, Z. Liu *et al.*, "Study on effect of different surface roughness on nanofluid flow in nanochannel by using molecular dynamics simulation," *J. Mol. Liq.* **346**, 117148 (2022).
- <sup>37</sup>A. P. Thompson, H. M. Aktulga, R. Berger *et al.*, "LAMMPS—A flexible simulation tool for particle-based materials modeling at the atomic, meso, and continuum scales," *Comput. Phys. Commun.* **271**, 108171 (2022).
- <sup>38</sup>Z. Zong, X. Chen, B. Yan *et al.*, "Theoretical models on interfacial thermal conductance of nanoscale solid interfaces in chips: A mini review," *Chin. Phys. Lett.* **41**(10), 106301 (2024).
- <sup>39</sup>A. Togo, L. Chaput, T. Tadano *et al.*, "Implementation strategies in phonopy and phono3py," *J. Phys.: Condens. Matter.* **35**(35), 353001 (2023).
- <sup>40</sup>X. Gu, Z. Fan, and H. Bao, "Thermal conductivity prediction by atomistic simulation methods: Recent advances and detailed comparison," *J. Appl. Phys.* **130**(21), 210902 (2021).
- <sup>41</sup>J. Li, P. Ying, T. Liang *et al.*, "Mechanical and thermal properties of graphyne-coated carbon nanotubes: A molecular dynamics simulation on one-dimensional all-carbon van der Waals heterostructures," *Phys. Chem. Chem. Phys.* **25**(12), 8651–8663 (2023).
- <sup>42</sup>P. Ying, T. Liang, K. Xu *et al.*, "Sub-micrometer phonon mean free paths in metal-organic frameworks revealed by machine learning molecular dynamics simulations," *ACS Appl. Mater. Interfaces* **15**(30), 36412–36422 (2023).
- <sup>43</sup>J. Han, B. Xu, M. Hu *et al.*, "Analytical study on the size effect of phonon spectral energy density resolution," *Comput. Mater. Sci.* **132**, 6–9 (2017).
- <sup>44</sup>J. Che, X. Liu, X. Wang *et al.*, "Fluctuating bonding leads to glass-like thermal conductivity in perovskite rare-earth tantalates," *Acta Mater.* **237**, 118162 (2022).
- <sup>45</sup>A. Stukowski, "Visualization and analysis of atomistic simulation data with OVITO—The Open Visualization Tool," *Modell. Simul. Mater. Sci. Eng.* **18**(1), 015012 (2010).
- <sup>46</sup>Z. Wu, M. Fan, Y. Qin *et al.*, "Achieving ultra-high anisotropy in thermal conductivity of plastic crystals through megapascal pressure via hot pressing," *J. Mater. Chem. C* (published online 2025).
- <sup>47</sup>S. Maruyama, "A molecular dynamics simulation of heat conduction of a finite length single-walled carbon nanotube," *Microscale Thermophys. Eng.* **7**(1), 41–50 (2003).



# Supplemental Material

## A significant enhancement in thermal conductivity of plastic crystals under compressive strain by deep potential molecular dynamics

Yangjun Qin<sup>1,2</sup>, Zhicheng Zong<sup>1,2</sup>, Junwei Che<sup>3</sup>, Tianhao Li<sup>1,2</sup>, Haisheng Fang<sup>1</sup>, Nuo Yang<sup>2, †</sup>

1) School of Energy and Power Engineering, Huazhong University of Science and Technology,

Wuhan 430074, China

2) Department of Physics, National University of Defense Technology, Changsha 410073, China

3) Department of Applied Physics, College of Science, Xi'an University of Science and Technology,

Xi'an, 710054, China

†Corresponding E-mail: N.Y. (nuo@nudt.edu.cn)

### I. Training details

For each of the four phases, 100 structure files were generated, with atomic positions perturbed by 0.001 nm. These structures were then subjected to ab initio molecular dynamics (AIMD) simulations at 300 K over 15 steps, yielding 4,500 initial data sets. The embedded network, fitted network, truncation radius, and `rcut_smth` were configured to (25, 50, 100), (240, 240, 240), 0.6 nm, and 0.5 nm, respectively. A total of 500,000 training steps were employed. The hyperparameters—`start-pref_e`, `start-pref_f`, `start-pref_v`, `limit-pref_e`, `limit-pref_f`, and `limit-pref_v`—were set to 0.02, 1000, 0.02, 1.0, 1.0, and 1.0, respectively.

In this study, the machine learning approach includes both potential function training and active learning components. Initially, potential models were trained using data generated under four different random seeds. One of these models was used to perform molecular dynamics (MD) simulations for exploring the structural space, while

the others were employed to validate the MD results. Training was considered complete when the accuracy reached 99% in each round. Due to the nature of the active learning process, it was not feasible to strictly define the ratio between the training and validation datasets.

The validation of the potential functions was primarily carried out by performing separate VASP calculations over a temperature range of 200 K to 400 K for 500 steps. The resulting data, including energies and forces, were used as a test set to assess the accuracy of the trained potentials.

Table S1: Exploration settings of DP-GEN iterations

Iter.	Structures	Length(ps)	T(K)	Pressure (bar)	Candidate (%)	Accurate (%)	Failed (%)	Total data
0	PhaseIV(44 atoms)+phase III(44 atoms)+V ( 88 atoms ) +VI(22atoms)	0.1(200)	200 300 330 360 420	0 10 100 1000 10000	31.3	65.40	3.31	21000
1		0.1(200)			9.49	88.64	1.87	21000
2		0.1(200)			3.45	96.55	0	21000
3		0.1(200)			3.55	96.45	0	21000
4		0.1(200)			1.64	98.36	0	21000
5		0.25(500)			43.89	56.00	0.10	51000
6		0.25(500)			15.05	84.78	0.16	51000
7		0.25(500)			12.15	87.81	0.03	51000
8		0.5(1000)			13.95	85.96	0.10	101000
9		0.5(1000)			12.59	87.30	0.12	101000
10		0.5(1000)			9.94	90.03	0.028	101000
11		0.5(1000)			4.86	95.12	0.02	101000
12		2.5(5000)			3.83	96.16	0.013	101000
13		2.5(5000)			1.44	97.65	0.91	101000
14	7.5(15000)	1.65	98.32	0.04	301000			

15		15(30000)			1.48	98.52	0.0015	401000
16		15(30000)			0.65	99.35	7.4813 E-4	401000

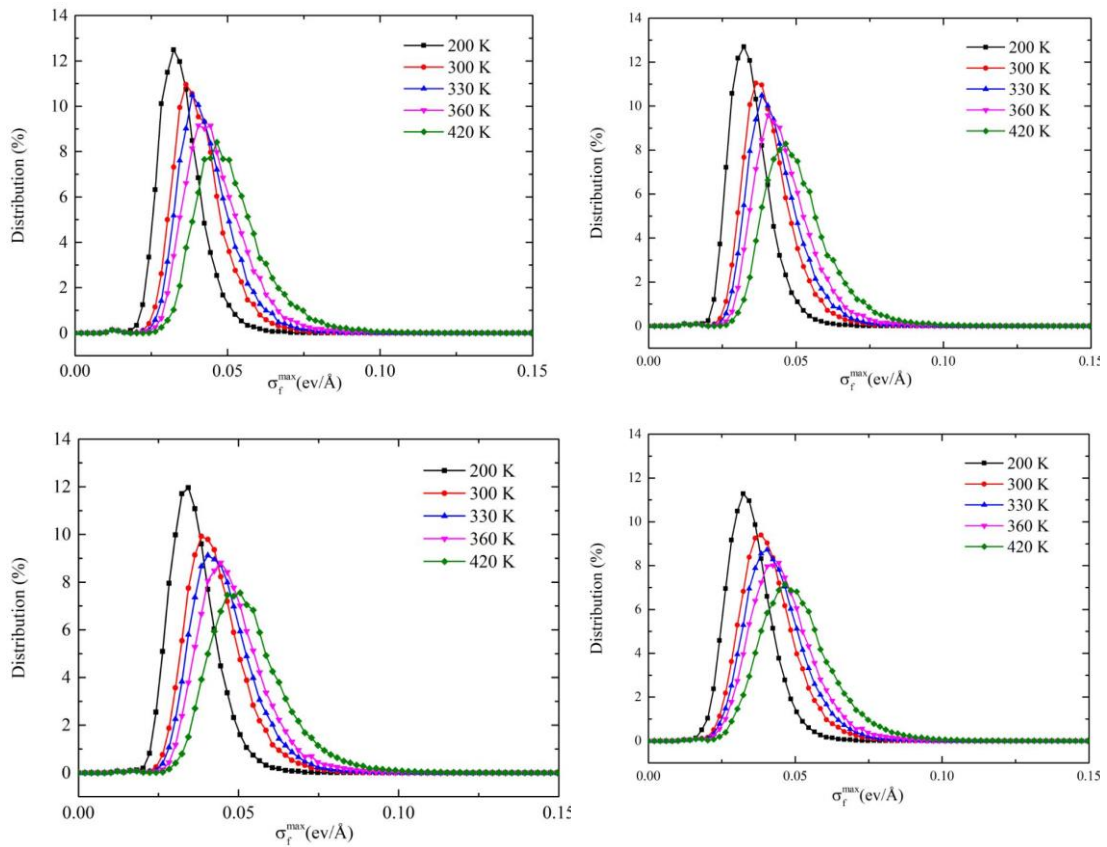


Figure S1 The maximum force deviation distribution for the four phases at the final iteration is presented herewith.

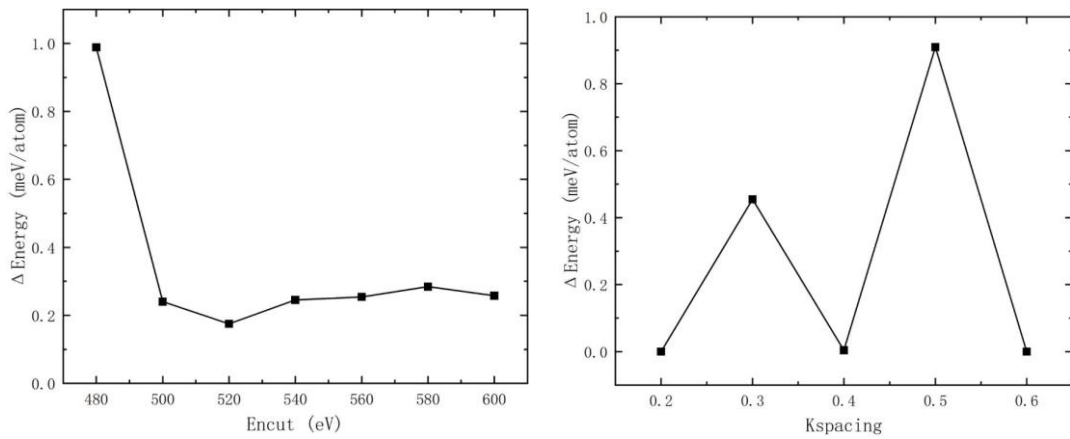


Figure S2 (a) The total energy differences to the kinetic energy cutoff; (b) The total energy differences to the k-point grid

## II. Simulation details

All molecular dynamics simulations were conducted using the LAMMPS software. A  $5 \times 4 \times 4$  supercell was constructed with lengths of 3.55 nm, 3.58 nm, and 3.63 nm in the [100], [010], and [001] directions of the system, respectively, with periodic boundaries in all three directions. The velocity-Verlet method was employed to iteratively solve Newton's equations, thereby obtaining the position and velocity information of the atoms. The time step employed for the simulation is 0.5 fs. Prior to the application of the strain, the initial model is subjected to an energy minimization process. Subsequently, the NPT ensemble is relaxed at 330 K and 1 atm for a duration of 0.5 ns, thereby facilitating the complete release of stresses within the system. The system was subjected to uniform strains, resulting in strains of 3%, 7%, and 9% in the [100], [010], and [001] directions, respectively. Subsequently, a 300K relaxation is conducted under NVT ensemble for 0.3 ns, followed by an additional run under NVE ensemble for 0.2 ns. Finally, data collection and statistical analysis are performed to calculate the heat flow and thermal conductivity.

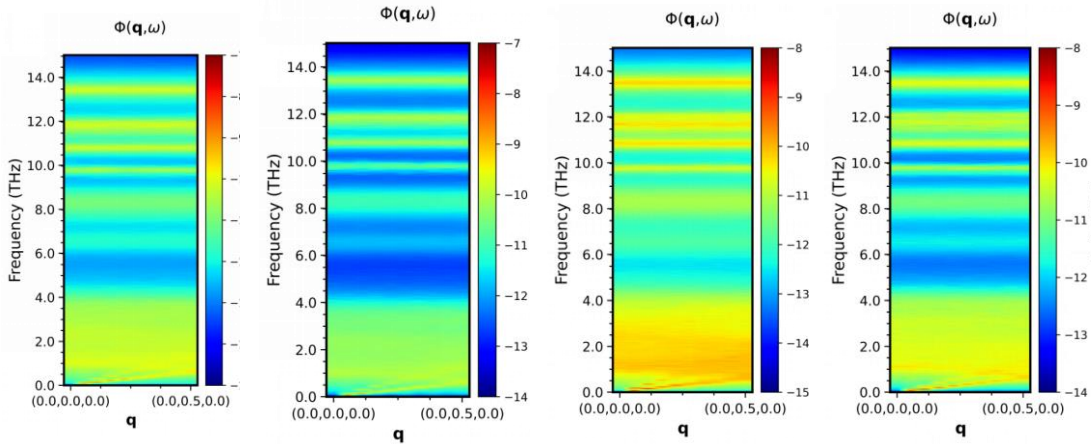


Figure S3. The normalized SED of PCs with strain of 0%, [100]-3%, [010]-7% and [001]-9% at 0-15 THz.

### III. The comparison of UFF and DP

The parameters of UFF utilized extensively are estimated based on elemental identity, hybridization, and connectivity<sup>[1]</sup>. Atom-atom interaction potentials were computed using the Lorentz-Berthelot mixing rules<sup>[2]</sup>, which offer only limited accuracy and fail to capture phase transitions, many-body effects, and electron transfer. In contrast, machine learning potentials, which provide density functional theory (DFT)-level accuracy and computational efficiency of classical force fields.

Firstly, the potential energy and volume were calculated using both UFF-CVFF MD and DPMD during the NPT relaxation (shown in Fig. S4). The system was fully relaxed and stabilized within 1 ns. It is also observed that the difference in potential energy calculated by UFF-CVFF MD and DPMD is nearly double. This is mainly due to the interaction forces of the atoms in the system, the state of the atoms and the truncation radius, etc. UFF-CVFF has a truncation radius of 12 Å, which allows a larger range of forces to be considered, while DP has a truncation radius of 6 Å<sup>[3]</sup>, which is sufficient for calculations of the general properties of the material.

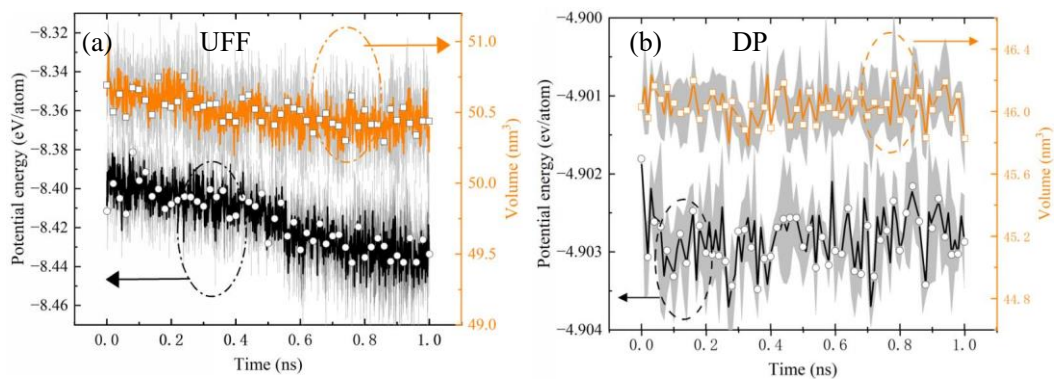


Fig.S4 (a) and (b) are the volume and potential energy diagrams under NPT ensemble, respectively. The shadow area is the error band. The white dots and rectangles correspond to

the potential energy and volume, respectively.

Secondly, the potential energy and volume were calculated using both UFF-CVFF MD and DPMD under different compress strains along the [001] direction in Fig. S5. It observed that there are significant differences between the two potential functions throughout the process. The DPMD method, by accurately capturing the response of system to strain, is particularly well-suited for investigating thermal transport properties under varying strain conditions. However, the calculation of potential energy and volume is performed using UFF-CVFF MD, which demonstrates a monotonic decrease.

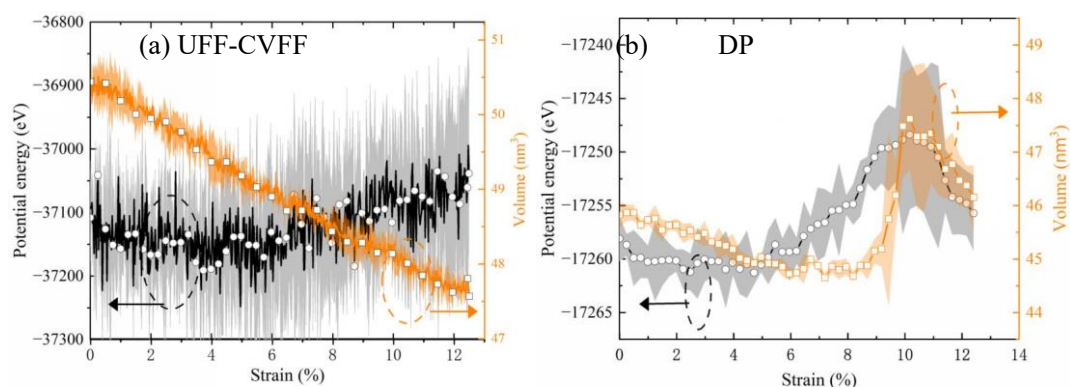


Fig.S5 The potential energy and volume under different compress strains along [001] direction using both (a) UFF-CVFF MD and (b) DPMD, respectively. The shadow area is the error band. The white dots and rectangles correspond to the potential energy and volume, respectively.

Thirdly, as shown in Fig. S6, the stress-strain curves were calculated using both UFF-CVFF MD and DPMD, which represents a significant tool for the description of the deformation behavior of materials under compress strain. The DPMD accurately modelled the three stages of the system under pressure: the elastic, plastic and rupture stages. The UFF-CVFF MD exists only in the elastic and plastic stages. Besides, the

structure was visualized under different strains in Fig.S7. The DPMD displays a structure that is more consistent with the crystal configuration, and its structural changes are also largely consistent with the stress-strain. The structure after relaxation with UFF-CVFF MD shows a certain degree of disorder, resulting in an unreasonable enhanced phonon scattering and reduced thermal conductivity.

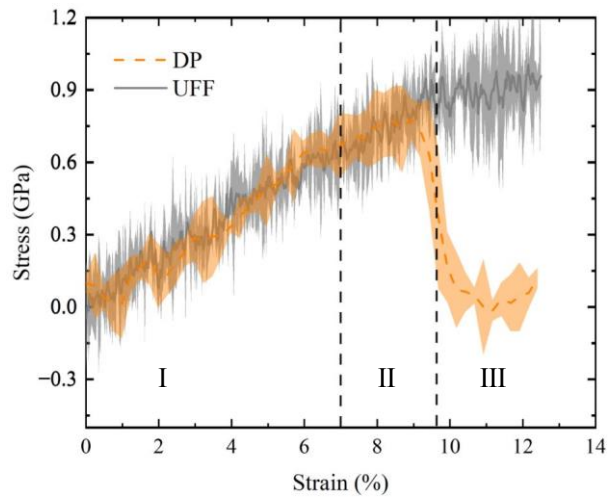
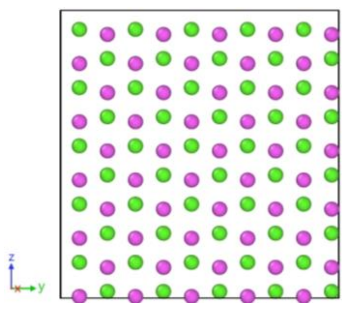
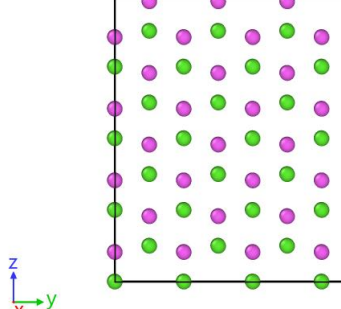
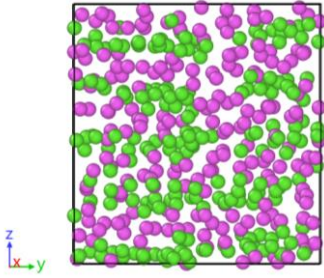
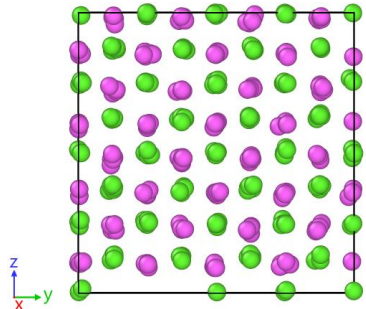
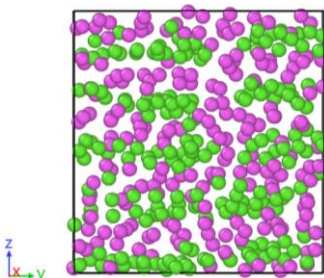
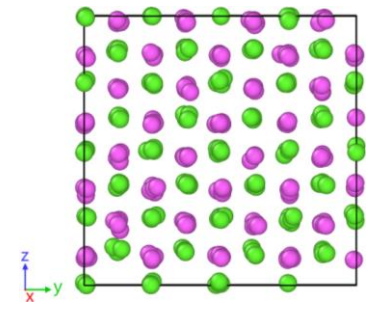
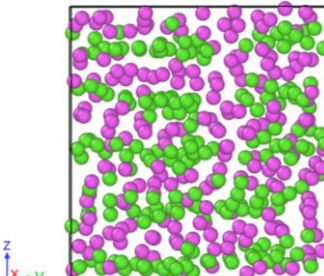
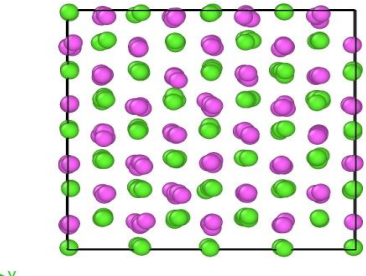
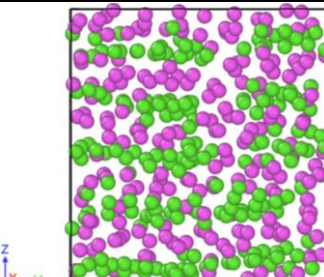
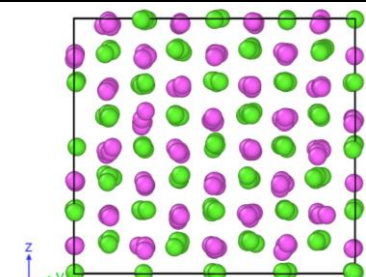
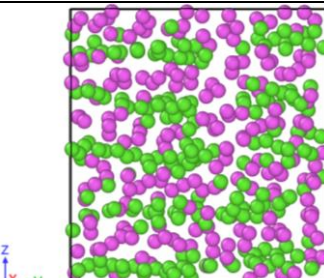
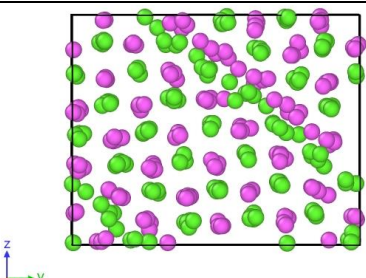


Fig.S6 Comparison of stress-strain under DPMD and UFF-CVFF MD. Shadow area is the error band. I, II, III are the three processes in strain, which are the elastic, plastic and rupture stages, respectively.

Strain	UFF-CVFF MD	DPMD
Initial structure		

Structure_ Relaxed		
1%		
6%		
9%		
10.8%		



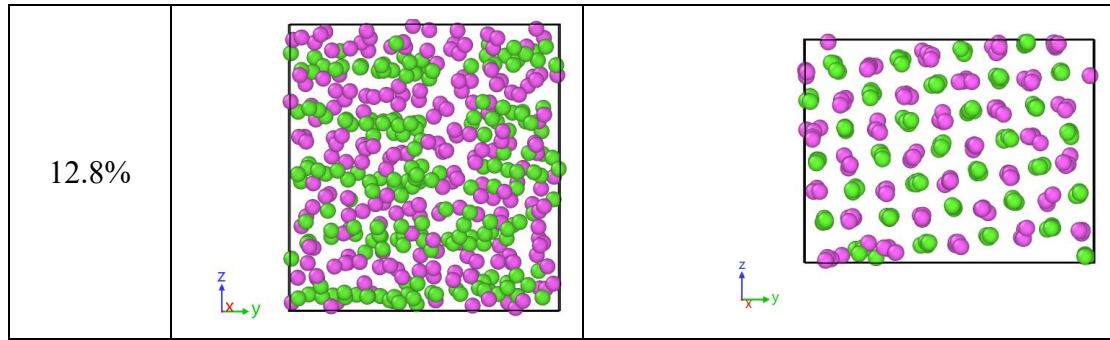


Fig. S7. The structure of  $[(\text{CH}_3)_4\text{N}][\text{FeCl}_4]$  simulated by DPMD and UFF-CVFF MD under different compressive strain along  $[001]$ . For the for easier visibility, it is only shown that iron atoms (pink) and nitrogen atoms (green).

Finally, the thermal conductivity was calculated and compared using UFF-CVFF MD and DPMD which is shown in Fig. 3d and Fig.S8. For the UFF-CVFF MD system, relaxation was conducted for 1 ns under NPT ensemble, followed by 0.5 ns under NVE ensemble. Finally, the system was run for 1.5 ns under NVE ensemble to complete the sampling of heat flux and the heat current autocorrelation function (HCACF). The time step was set to 0.25 fs. Details regarding the potential functions used are provided in Ref. <sup>[4]</sup>. Ten cases were simulated, and thermal conductivity data within the correlation time range of 2 ps to 10 ps were averaged. As shown in Fig. S8(c), the simulation setup is validated as reasonable.

It is compared that the thermal conductivity of the system at 0% strain, calculated using both DPMD and UFF-CVFF MD. In Ref.<sup>[4]</sup>, only in-plane and out-of-plane thermal conductivity values are measured. The in-plane thermal conductivity (along  $[100]$  and  $[010]$ ) value is measured as 0.16 W/m-K. As shown in Fig.S6(a)-(b), the thermal conductivity of the system under ambient conditions exhibits notable anisotropy, with simulations aligning well with experimental results. The simulated

thermal conductivity values are slightly higher than the experimental values, primarily due to defects such as grain boundaries and voids in the experimental materials, which enhance phonon scattering and lower thermal conductivity.

The thermal conductivity was calculated using the UFF-CVFF MD and DPMD along the [001] direction at 9% strain in Fig. S8 (a). The results show significant increases of 580%, 114%, 408% and 268% using DPMD in the [010], [001] [101] and [011] directions, respectively. Whereas, the improvements with the UFF-CVFF potential are much less pronounced. This discrepancy is primarily due to the inability of UFF-CVFF to capture structural changes, failing to reflect phenomena such as system collapse under strain.

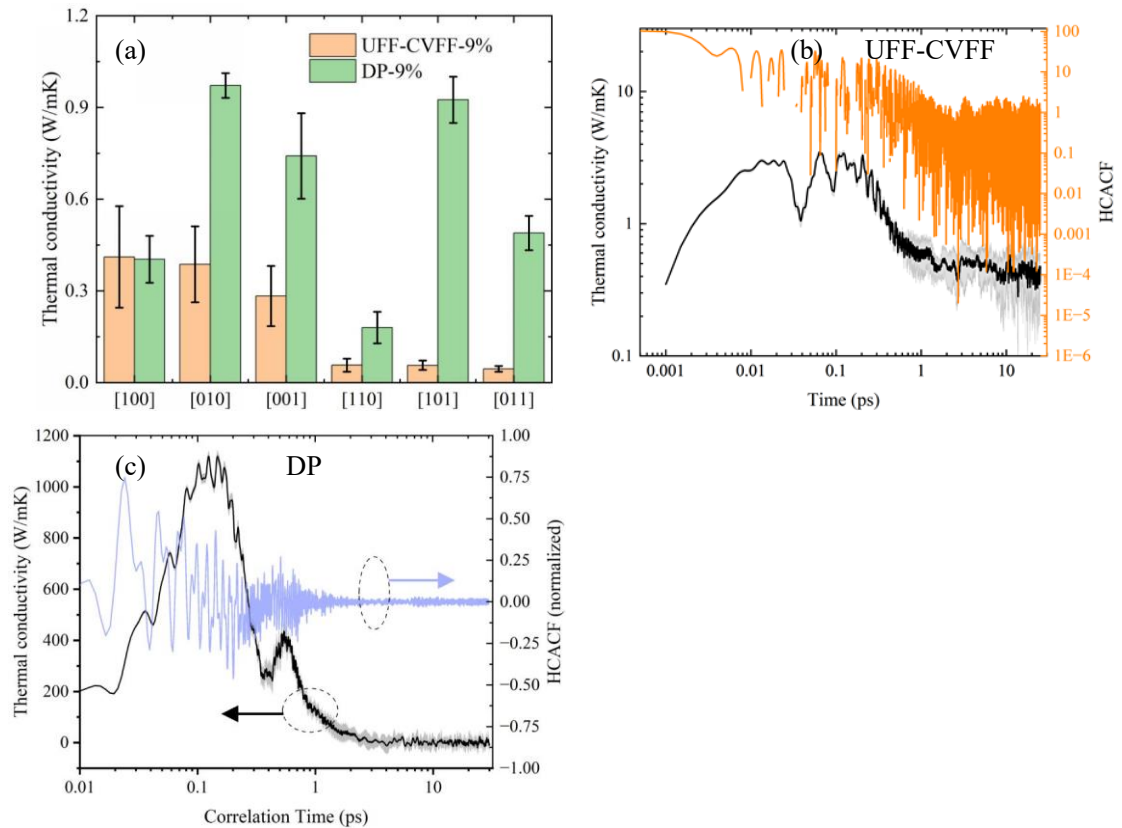


Fig.S8 (a) The thermal conductivity of PC was compared by UFF-CVFF MD, DPMD and experiment, respectively along [001] direction under 9% strain. (b)-(c) The

HCACF and the thermal conductivity of PCs as a function of correlation time along [001] direction under 9% strain using UFF-CVFF MD and DPMD, respectively.

#### IV: The Analysis of MSD

The MSD is calculated in terms of the following expression:

$$MSD(t) = \langle |r_i(t) - r_i(0)|^2 \rangle$$

where  $t$  is the simulation time,  $r$  represents the position of the atom.

The MSD distributions for different atoms in the absence of strain are depicted in Fig. S9(a), where it is evident that hydrogen atoms exhibit significantly higher MSD compared to other atoms. The heavier Fe atoms, along with the low-frequency vibrations of the Cl atoms, play a more prominent role in thermal transport. Furthermore, the radial distribution functions of Fe and N at varying strains are presented in Fig.S9(b), demonstrating a redistribution of the lattice structure at high strains. The application of high strain mainly changes the vibrational modes of the massive atoms, weakens the phonon scattering, and enhances the thermal conductivity of the PCs.

The MSD of Cl and Fe atoms at 0% and 9% strain was calculated (see Fig.S9(c)-(f)). It was found that Cl atoms exhibit localized rotational diffusion at 0% strain, and that the rate of diffusion increases with the application of 9% strain. The rapid rotational diffusion in anions leads to diffusion jumps in cations, a phenomenon that has been observed in ionic plastic crystals<sup>[5]</sup>.

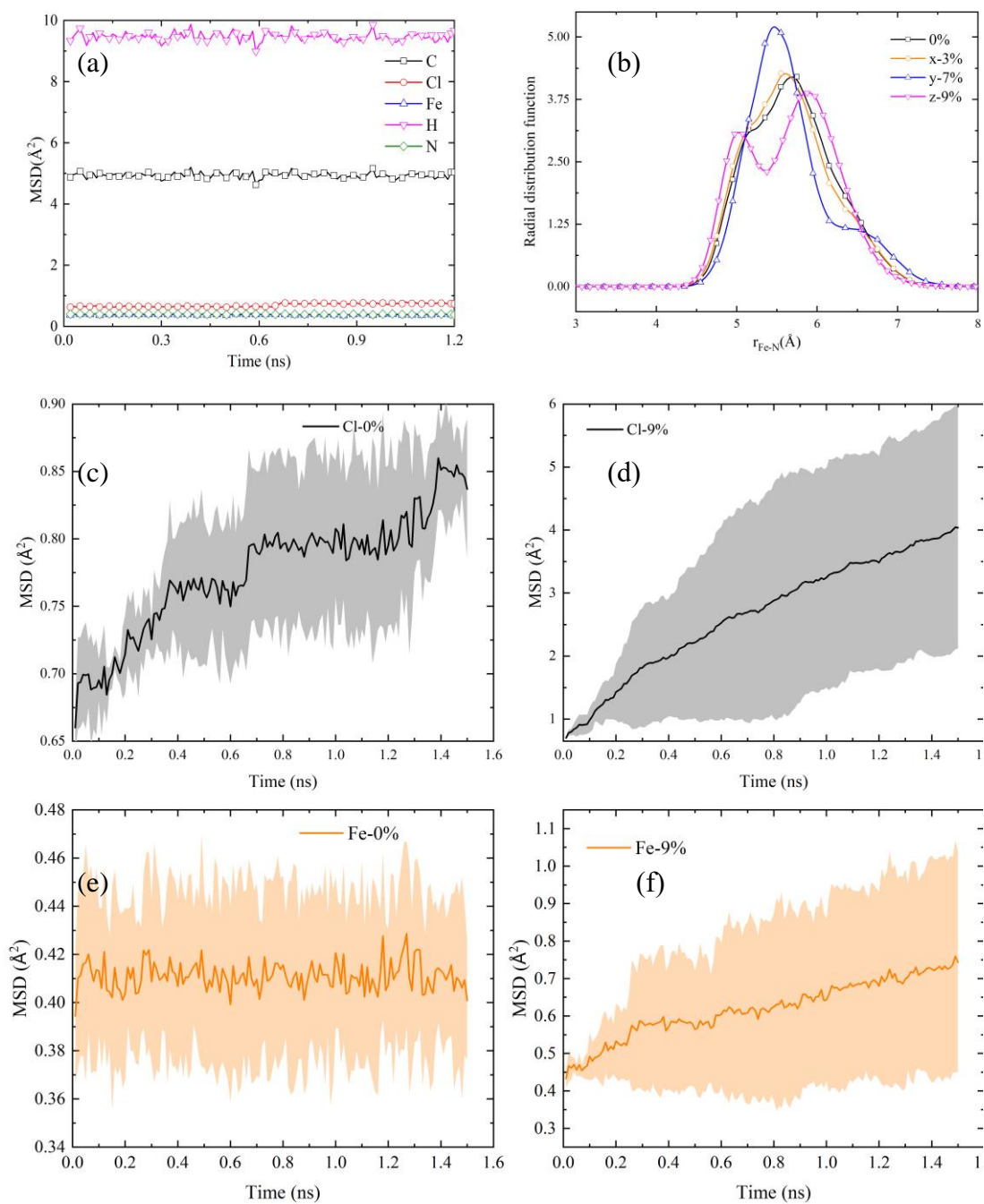


Figure S9. (a)MSD distribution of different atoms under 0% strain along [001] direction. (b)RDF profile of different atoms. (c) the MSD of Cl atoms under 0% strain along [001] direction. (d) the MSD of Cl atoms under 9% strain along [001] direction. (e) the MSD of Fe atoms under 0% strain along [001] direction. (f) the MSD of Fe atoms under 9% strain along [001] direction.

## Reference

- [1] Rappe, A.K., C.J. Casewit, K.S. Colwell, W.A. Goddard, III, and W.M. Skiff, UFF, a full periodic table force field for molecular mechanics and molecular dynamics simulations. *Journal of the American Chemical Society*, 1992. **114**(25): p. 10024-10035.
- [2] Lorentz, H.A., Ueber die Anwendung des Satzes vom Virial in der kinetischen Theorie der Gase. *Annalen der Physik*, 1881. **248**(1): p. 127-136.
- [3] Tisi, D., L. Zhang, R. Bertossa, H. Wang, R. Car, and S. Baroni, Heat transport in liquid water from first-principles and deep neural network simulations. *Physical Review B*, 2021. **104**(22): p. 224202.
- [4] Wu, Z., M. Fan, Y. Qin, G. Zhang, and N. Yang, Achieving ultra-high anisotropy in thermal conductivity of plastic crystals through megapascal pressure via hot pressing. *Journal of Materials Chemistry C*, 2025.
- [5] Zhang, Z. and L.F. Nazar, Exploiting the paddle-wheel mechanism for the design of fast ion conductors. *Nature Reviews Materials*, 2022. **7**(5): p. 389-405.